

Selenium Nanocomposite Cathode with Long Cycle Life for Rechargeable Lithium-Selenium Batteries

Yi Cui,^[a, c] Xinwei Zhou,^[a, c, d] Wei Guo,^[b] Yuzi Liu,^[d] Tianyi Li,^[a, c] Yongzhu Fu,^{*[b]} and Likun Zhu^{*[a]}

Selenium (Se) is a potential cathode material for high energy density rechargeable lithium batteries. In this study, a binder-free Se-carbon nanotube (CNT) composite electrode has been prepared by a facile chemical method. At initial state, Se is present in the form of branched nanowires with a diameter of < 150 nm and a length of 1–2 μm , interwoven with CNTs. After discharge and re-charge, the Se nanowires are converted to nanoparticles embedded in the CNT network. This synthesis method provides a path for fabricating the Se cathodes with controllable mass loading and thickness. By studying the

composite electrodes with different Se loading and thickness, we found that the electrode thickness has a critical impact on the distribution of Se during repeated cycling. Promising cycling performance was achieved in thin electrodes with high Se loading. The composite electrode with 23 μm thickness and 60% Se loading shows a high initial capacity of 537 mAh g^{-1} and stable cycling performance with a capacity of 401 mAh g^{-1} after 500 cycles at 1 C rate. This study reports a synthesis strategy to obtain Se/CNT composite cathode with long cycle life for rechargeable Li–Se batteries.

1. Introduction

In the past two decades, lithium-ion batteries (LIBs) have been extensively utilized in portable electronic devices as well as electric vehicles (EVs).^[1] However, conventional LIBs depending on the lithium intercalation reactions of anode and transitional metal oxide cathode materials have limited capacities and low energy densities, which prevent their broader deployment as power sources for prolonged usage.^[2] High energy density and durable electrical energy storage devices are the key factors to meet the crucial demands for high-performance portable electronic devices and EVs. Lithium-sulfur (Li–S) batteries have attracted particular interest and been proposed as the next-generation rechargeable systems, due to the high theoretical specific capacity (1672 mAh g^{-1}) and high theoretical energy density (2600 Wh kg^{-1}) of sulfur.^[3] In addition, the characteristics of sulfur such as low cost, abundance, and environmental

benignity make it attractive to be an electrode material.^[4] Despite these advantages, Li–S batteries are facing challenges toward practical applications, including the insulating nature of sulfur ($5 \times 10^{-28} \text{ Sm}^{-1}$), large volume change (up to 80%) upon cycling, so-called shuttle effect and active materials loss over repeated cycling.^[5] Various strategies have been developed to address these challenges, including using carbon matrix hosts,^[6] utilizing optimized electrolyte,^[7] constructing carbon layers,^[8] and adjusting functional polymers.^[9] However, the intrinsic weaknesses of Li–S batteries have not been completely solved.

Selenium (Se), as a congener of sulfur in the periodic table, has been proposed as an alternative cathode material for rechargeable lithium batteries. Although Se has lower theoretical capacity (678 mAh g^{-1}) than sulfur, it can provide a high volumetric capacity of 3253 mAh cm^{-3} because of its high mass density (4.8 g cm^{-3}).^[10] In addition, selenium has a much higher electronic conductivity ($1 \times 10^{-3} \text{ Sm}^{-1}$), which implies that Se could provide better electrochemical activity.^[11] However, Se cathode is still facing similar challenges as sulfur such as poor cycling life and low Coulombic efficiency, which are attributed to the dissolution and shuttle effect of the formed high-order polyselenides as redox intermediates in the ether-based electrolyte. In addition, the significant volume change increases the difficulty for Li–Se batteries to be used in practical applications.^[12] During the last decade, lots of effort have been put into developing approaches to address these problems, thereby increasing energy density and cycle life of Li–Se batteries.^[13] For instance, Zhang et al. sealed Se nanowires by polyaniline to form core-shell structure and then encapsulated the composite material using graphene to improve the cycling performance.^[14] Zeng et al. confined Se in 3-dimensional interconnected mesoporous carbon nanofibers as a flexible and binder-free electrode.^[15] He et al. added carbon nanotubes/Se

[a] Y. Cui, X. Zhou, T. Li, Prof. L. Zhu
Department of Mechanical and Energy Engineering
Indiana University-Purdue University Indianapolis
Indianapolis, IN 46202, United States
E-mail: likzhu@iupui.edu

[b] Prof. W. Guo, Prof. Y. Fu
College of Chemistry and Molecular Engineering
Zhengzhou University
Zhengzhou 450001, P. R. China
E-mail: yfu@zzu.edu.cn

[c] Y. Cui, X. Zhou, T. Li
School of Mechanical Engineering
Purdue University
West Lafayette, IN 47907, United States

[d] X. Zhou, Dr. Y. Liu
Center for Nanoscale Materials
Argonne National Laboratory
Argonne, Illinois 60439, United States

 Supporting information for this article is available on the WWW under <https://doi.org/10.1002/batt.201900050>

between graphene layers to form high performance binder-free Se cathodes.^[16]

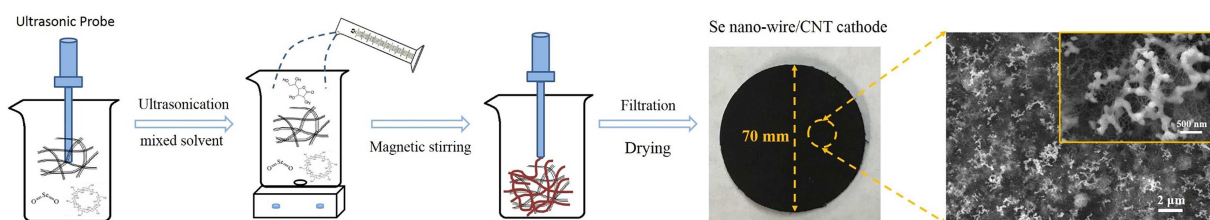
In this contribution, we synthesized Se nanowires in the presence of carbon nanotubes (CNTs) by a facile method. Se nanowires are weaved with CNTs to form a uniform binder-free composite electrode, which has superior electrical conductivity. This synthesis method provides a path for fabricating the Se cathodes with controllable mass loadings and thicknesses. By studying the composites electrodes with different mass loadings of active materials and different thicknesses, it is found that the electrode thickness has influence on the accumulation of redox products upon repeated cycling. The structural and morphological changes are analyzed by scanning electron microscope (SEM). Finally, the electrochemical phenomena are revealed experimentally, and enhanced cycling performance is achieved.

2. Results and Discussion

The experimental process for preparing the Se/CNT composite is schematically illustrated in Scheme 1 (see the experimental section for a detailed process description). The process consists of dissolving selenium oxide (SeO_2) and beta-cyclodextrin (β -cyclodextrin) and dispersing the CNT bundles in an ethanolic mixture with de-ionized water. The vigorously stirring and ultrasonication procedure in the initial mixture cause fine dispersion of CNTs. In addition, the ethanol extenuates the hydrophobic activity of CNTs, and hence accelerates the dispersion-weave process by ultrasonication. The addition of ascorbic acid solution ensures the product of selenium nano-

wires. The synthesized selenium nanowires are effectively confined and encapsulated by the interwoven CNTs as precipitations out of the solution. Upon another ultrasonication for selenium nanowires and CNTs to be perfectly woven, and then filtered and dried, the Se/CNT composite electrode was obtained. The filter paper has a diameter of 7 cm, which decides the overall size of the composite electrode. SEM was performed to examine the morphology of the composite, as shown in Scheme 1. The SEM image shows that the synthesized selenium nanowires are completely encapsulated by CNTs, leading to a uniformly distributed composite. The inset magnified SEM image reveals that the selenium products are long nanometer-sized wires with uniform diameters, interweaving with CNTs. Electron dispersive spectroscopy (EDS) was also performed to investigate the elemental distribution, as shown in Figure S1. The EDS reveals the distribution of carbon and selenium elements in the composite cathode.

The structural estimation of the synthesized selenium nanowires is taken from the transmission electron microscopy (TEM) image in Figure 1a. The synthesized selenium was ultrasonicated in a solvent for obtaining single and detached nanowires. The size of the selenium nanowires is approximately 120 nm in diameter. Figure 1b shows a high resolution TEM (HRTEM) image of the marginal region of a selenium nanowire, which is highlighted by the yellow square and arrow. In the crystalline part, the observed fringe spacing is 0.327 nm, which agrees well with the lattice spacing of the (100) planes of selenium, confirming that the as-selected region is single crystal in the cylindrical margin. The corresponding selected area electron diffraction (SAED) of the as-prepared selenium nanowires is shown in Figure 1c. The SAED image exhibits



Scheme 1. Experimental procedure for the synthesis of the selenium nanowire/CNT composite electrode, with the SEM image showing the morphology of the composite electrode.

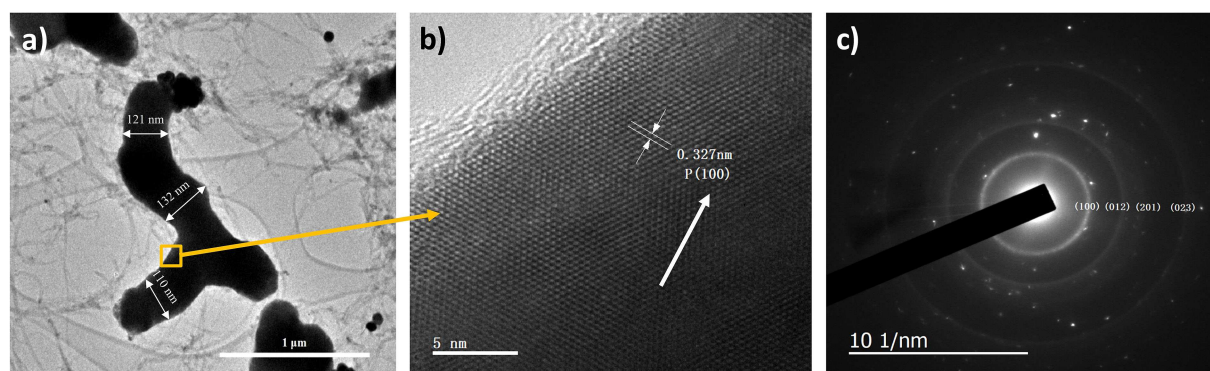


Figure 1. a) TEM image, b) HRTEM image and c) SAED pattern of the synthesized selenium nanowires.

diffraction rings corresponding to the (100), (012), (201) and (023) planes of the cylindrical phase, which confirms that polycrystallinity of the as-prepared selenium nanowires.

To further characterize the Se/CNT composite, thermogravimetric analysis (TGA) and differential scanning calorimetry (DSC) were performed. Two sets of the composites were prepared by adjusting the reactant amounts and regulating the vacuum filtration, the first set of composite electrodes are named as SeCE-1 and SeCE-2, and the second set of the thin composite electrode is named as TSeCE. The TGA was firstly performed to confirm the selenium nanowires loading in each set of the composite cathodes. Figure 2a shows the TGA plot for SeCE-2, which reveals that the selenium nanowires constitute approximately 61 wt.% in the composite. The TGA plots for SeCE-1 and TSeCE are shown in Figure S2, which reveal that the mass components of selenium nanowires are approximately 43 wt.% and 60 wt.%, respectively. SeCE-2 and TSeCE are chosen as the primary samples in this study because they have similar high selenium loading percentage and much discrepancy in thickness. According to the TGA results, the mass loadings of the selenium nanowires in the composite cathodes are 1.3 mg cm^{-2} in SeCE-1, 2.3 mg cm^{-2} in SeCE-2, and 0.88 mg cm^{-2} in TSeCE, respectively. The DSC spectra in Figure S3 show that the pure selenium nanowires exhibit a narrow

endothermic peak at 221–239 °C. The endothermic peak is attributed to the melting process. The melting points of the composite cathodes are in the order of SeCE-1 (195 °C) < TSeCE (204 °C) < SeCE-2 (207 °C) < selenium nanowires (221 °C).

The cross-section morphology of the initial SeCE-2 cathode is shown in the SEM image in Figure 2b. The thickness of the SeCE-2 cathode is approximately 82 μm. The selenium nanowires are well covered and stored by interweaving with CNTs. Chemical transformations are tracked using XRD patterns, as shown in Figure 2c. The synthesized composite cathode shows two major peaks of the (100) and (101) planes and peaks of the (102) and (201) planes with low intensities. Upon discharge, new peaks at 20° of 23°, 28° and between 37–43°, reveal the formation of Li₂Se. Upon charging, the selenium peaks reappear having higher intensities, especially the peaks of the (101) and (102) planes, which indicates a change in particles size and crystallinity upon cycling. After repeated cycling, major crystalline peaks of the (101), (102) and (003) planes of selenium appear. The cycling performance of SeCE-1 and SeCE-2 is shown in Figure S4. Both SeCE-1 and SeCE-2 have continuous capacity fading in the first 30 cycles. The SeCE-1 has a relatively stable cycling performance for over 100 cycles and higher capacity retention than SeCE-2 due to its low selenium loading.

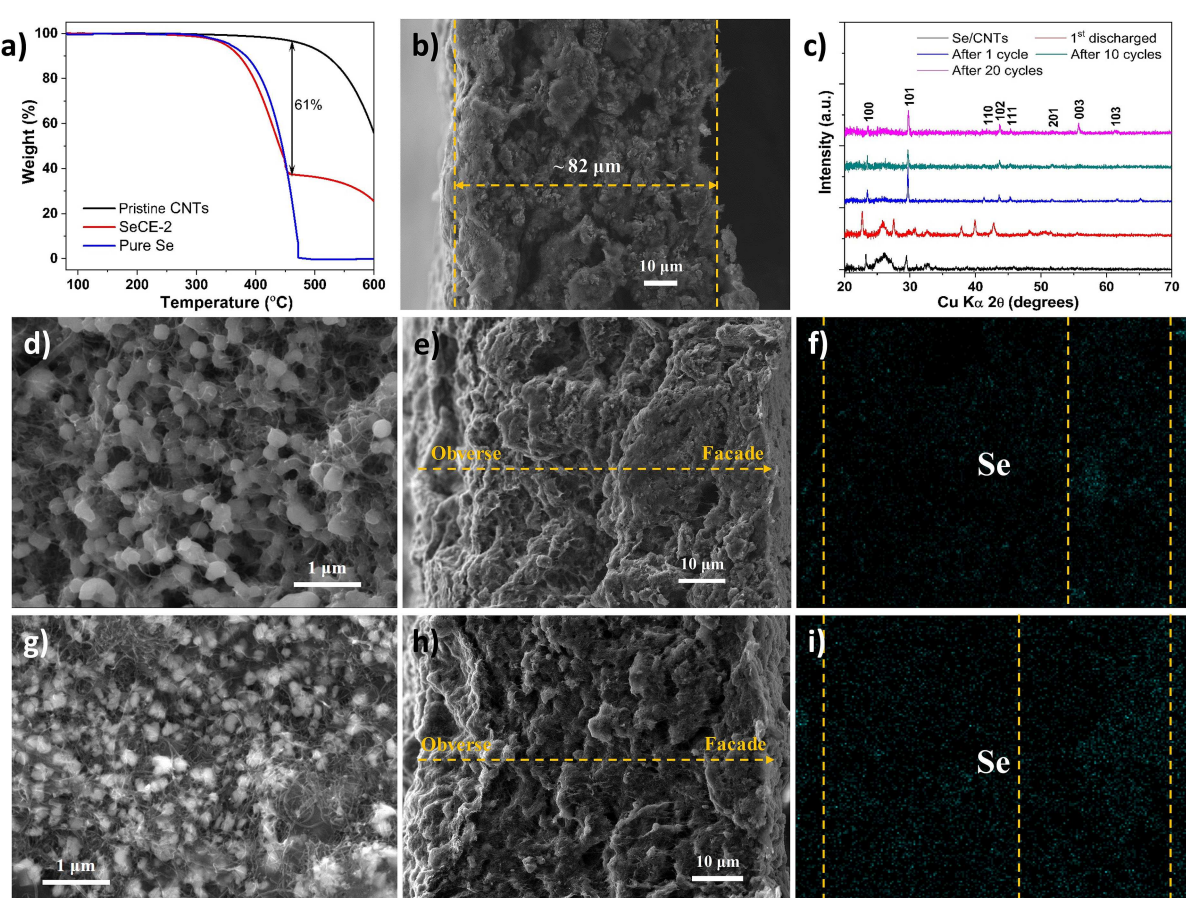


Figure 2. a) TGA plots and b) cross-section SEM image of the initial SeCE-2, c) XRD patterns of the composite electrode at different states of cycling, d) surface SEM image, e) cross-section SEM image, f) EDS showing selenium of the SeCE-2 at the discharged state, g) surface SEM image, h) cross-section SEM image and i) EDS showing selenium of the SeCE-2 at the charged state.

To evaluate the reasons causing the capacity fade, SEM was used to characterize the morphological changes after discharge and charge. The SEM image of the discharged electrode in Figure 2d shows that the discharge product of Li_2Se is not in nanowire structure. Instead, the selenium nanowires break into parts upon discharge, and the formed Li_2Se are nanometer-sized particles stored in the porous CNT network. The low magnified SEM image and elemental mappings of selenium, carbon and oxygen at electrode surface are shown in Figure S5, which reveal the distribution of Li_2Se as nanometer-sized particles in the CNT network structure. Upon discharge, the selenium nanowires undergo a solid-liquid phase transformation to form lithium polyselenides, which are soluble in the electrolyte. The continuous reduction leads a liquid-solid phase transformation to form insoluble Li_2Se which are in the particle format. The elemental mapping of selenium in Figure 2f shows that Li_2Se mainly precipitates on the facade side of the electrode in contact with the separator upon discharge. The selenium density within approximate 30% thickness of the facial side is visually higher than the density in the deep electrode, which means most CNTs are no longer able to store active material. If we consider the high loading area has 2 times selenium of that in the low loading area, the estimated mass loading of the selenium at the facade side can be up to 78%. The suddenly increased loading would result in difficulty in the conversion reactions between solid phase (Li_2Se) and liquid phase (polyselenides). The possible reason for the non-uniform distribution of Li_2Se in the composite electrode upon discharge could be the migration of anions of polyselenides to the separator side. During discharge, a lithium ion concentration gradient from lithium foil electrode (high) to the selenium electrode (low) is generated. To maintain charge neutrality, the anions of polyselenides tends to diffuse to the separator side, thereby generating a concentration gradient of polyselenides. The higher concentration of polyselenides on the separator side will result in more Li_2Se precipitation. The carbon mapping and the oxygen mapping of the cross-section are shown in Figure S6, which are mainly captured from CNTs and lithium salt. The recharged composite electrode was also reviewed by SEM and EDS.

In the charged state, the selenium nanowires are not regenerated, but in the particle format, as shown in the SEM images in Figure 2g. Figure S7 shows the low magnified SEM image and elemental mappings of selenium, carbon and oxygen, in which the distributions of selenium and lithium salt are demonstrated. The reversible solid-liquid-solid transformation happens during charging, which results in the formation of nanometer-sized selenium particles after the 1st cycle. As shown in the SEM image and selenium mapping in Figure 2h and i, much selenium is restored back to the obverse side of the CNT paper, but the selenium concentration gradient still slightly exists. Approximately half of the composite electrode has a higher selenium distribution. The carbon mapping and the oxygen mapping captured from CNTs and lithium salt are shown in Figure S8. This phenomenon can also be explained by charge neutrality. During charge, a lithium ion concentration gradient from the selenium electrode (high) to lithium foil

electrode (low) is generated, which is opposite to the discharge process. To maintain charge neutrality, the anions of polyselenides tends to diffuse to the selenium electrode, thereby decreasing the concentration gradient of polyselenides. The highly increased surface loading causes the difficulty for Li_2Se being recharged and reduce the utilization of the active materials, herein causing continuous capacity fades during prolonged cycling.

To avoid this uneven distribution of selenium during redox process, the thickness of the composite electrode is highly decreased for TSeCE, while the same material loading in the composite electrode is maintained. We hypothesize that the concentration gradient of polyselenides can be decreased in the thinner selenium electrode and the issue of uneven distribution of selenium can be addressed. The loading result of TSeCE is shown in the TGA plot of Figure S2. The SEM image of the cross-section of TSeCE is shown in Figure 3a. It can be seen that the selenium nanowires are completely encapsulated by the CNTs interwoven network structure. The thickness is approximately 23 μm measured by SEM. From the TGA plots, we can confirm that the mass percentages of selenium for TSeCE and SeCE-2 are almost the same. The initial selenium nanowires are uniformly distributed in the CNTs, which is also demonstrated by the selenium mapping in Figure 3b. The overlap mapping and carbon mapping are shown in Figure S9. The SEM image of the cross-section after discharge in Figure 3c shows that the formed Li_2Se particles are uniformly distributed in the CNTs network. The elemental distributions were scanned by EDS, in which the selenium mapping shows uniform distribution of selenium in the CNT network (Figure 3d). Upon charging, both the SEM image and the selenium mapping in Figure 3e and f show a uniform distribution of the reversed selenium in the composite electrode. The carbon mapping and oxygen mapping for discharged state and charged state are shown in Figure S10 and S11, respectively. In both discharged and charged states, no obvious selenium concentration gradient is observed for this thinner electrode. After redox reactions, the products are still uniformly distributed in the composite electrode. The maintained contacts between selenium and CNTs provide a possibility for better performance during the repeated conversion reactions.

The TSeCE electrode was cycled at 1 C to test its cycling performance. As shown in Figure 4a, although the initial discharge specific capacity is 238 mAh g^{-1} , it increases to a specific capacity of 537 mAh g^{-1} in the second cycle, which is corresponding to about 79% of the theoretical capacity. After that, the specific capacity continuously fades to 477 mAh g^{-1} in the first 20 cycles and retains 401 mAh g^{-1} over 500 cycles, which is corresponding to 0.03% capacity fading per cycle. The capacity fading in the first several cycles could be due to the shuttle effect of the polyselenides. It takes few cycles for LiNO_3 to be reduced and form a stable passivation layer on the lithium metal electrode. The Coulombic efficiency (CE) is 65% initially, then keeps increasing to 93% in the following cycle. With the stable cycling, the CE consistently remains over 98% throughout 500 cycles. This indicates the active material loss is minimal during the stable cycling. The voltage profile for the

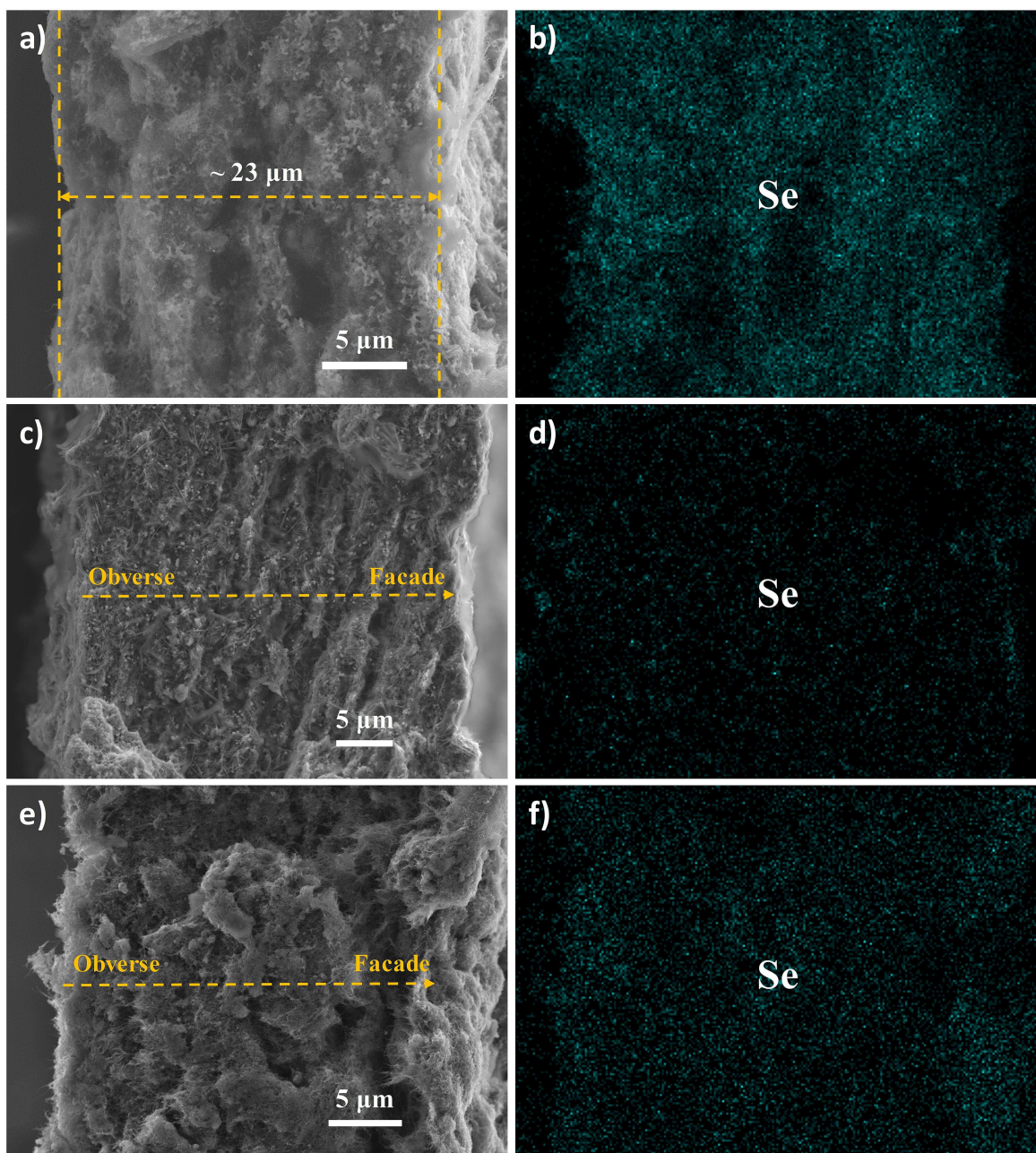


Figure 3. a) Cross-section SEM image, b) EDS showing selenium of the initial TSeCE, c) cross-section SEM image, d) EDS showing selenium of the TSeCE at the discharged state, e) cross-section SEM image and f) EDS showing selenium of the TSeCE at the charged state.

cell is shown in Figure 4b. Starting from the open-circuit voltage (OCV), the 1st discharge does not show two clear plateaus due to the incomplete discharge, and the charging plateaus are longer because of the polyselenides shuttle effect resulting in low CEs and longer charging process. In the following cycles, the first discharge plateau occurs at 2.04 V followed by further reduction plateau at 1.9 V. The charging step has two oxidation plateaus at 2.2 V and 2.37 V.

Figure 4c shows the cyclic voltammetry (CV) profiles of the composite cathode in the voltage range of 1.8–2.8 V with a sweep rate of 0.02 mVs⁻¹. In the initial cycle, the reduction peaks are shown at 2.11 and 1.94 V, corresponding to the

reduction from Se to polyselenides and the reduction from polyselenides to Li₂Se. The subsequent anodic scan exhibited two sharp anodic peaks at 2.22 and 2.27 V, corresponding to the reversible conversion from Li₂Se to polyselenides, and then to elemental selenium, respectively. The cathodic scan of the CV profiles remained unchanged after the first cycle. The anodic peaks after the 1st cycle move to slightly lower potential, in which the over potential is also decreased. The CV profiles indicate an excellent reversibility of the selenium nanowires in the composite cathode. The composite electrode is also tested under variable C-rates, as shown in Figure 4d. The composite electrode shows an initial specific capacity of 608 mAh g⁻¹ at C/

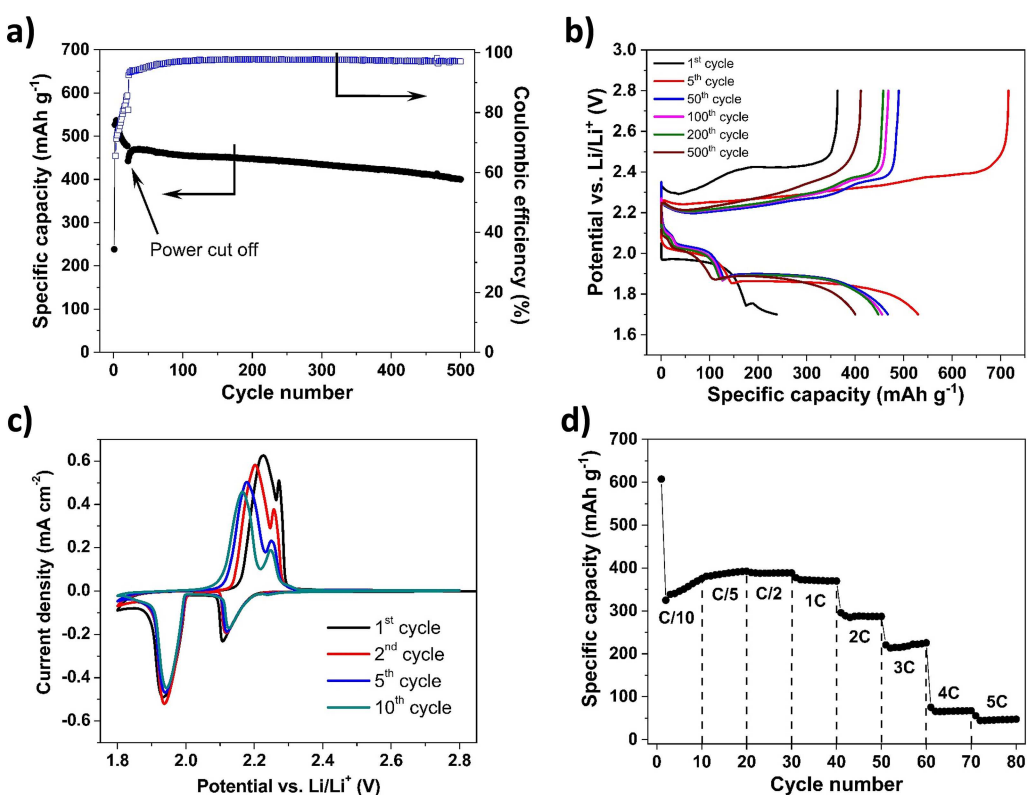


Figure 4. a) Cycling performance of the TSeCE at 1 C rate, b) voltage profile, c) cyclic voltammogram and d) rate performance of the TSeCE in rechargeable lithium batteries.

10 and 380 mAh g⁻¹ at C/5. The cell exhibits stable cycling performance with a specific capacity of 392 mAh g⁻¹ at C/2, 377 mAh g⁻¹ at 1 C, 295 mAh g⁻¹ at 2 C and 220 mAh g⁻¹ at 3 C, not having much capacity fades. When the cycling is further raised to higher C-rates, the cell retains the capacity of 75 mAh g⁻¹ at 4 C and 55 mAh g⁻¹ at 5 C.

Figure 5 compares the Nyquist plots of SeCE-2 and TSeCE initially, after the first discharge, and after the first charge, respectively. The intercepts of Nyquist plots in the high-frequency regions are 22.6 ohms for SeCE-2 and 10.2 ohms for TSeCE, which attribute to the bulk resistance of the liquid electrolyte. Both plots display one semicircle which are assigned to the charge transfer resistance (R_{ct}). The semicircle of the TSeCE is initially larger than that of SeCE-2 in the high-

medium frequency regions, for which the TSeCE initially has a higher charge transfer resistance than that of SeCE-2. The inset picture shows the equivalent circuit. In the Nyquist plots after discharge (Figure 5b), the intercepts of Nyquist plots are 18.7 ohms for SeCE-2 and 8.5 ohms for TSeCE. In addition, the charge transfer resistance of SeCE-2 is increased almost 3 times to approximately 460 ohms, while the charge transfer resistance of TSeCE is increased only 40% to about 460 ohms. As shown in Figure 5c, the intercepts are nearly the same after charging. But the charge transfer resistance of SeCE-2 is further increased to 940 ohms, while the charge transfer resistance of TSeCE is about 570 ohms. The impedance results show that the thinner electrode has relatively stable charge transfer resistance while the charge transfer resistance of thicker electrode keeps

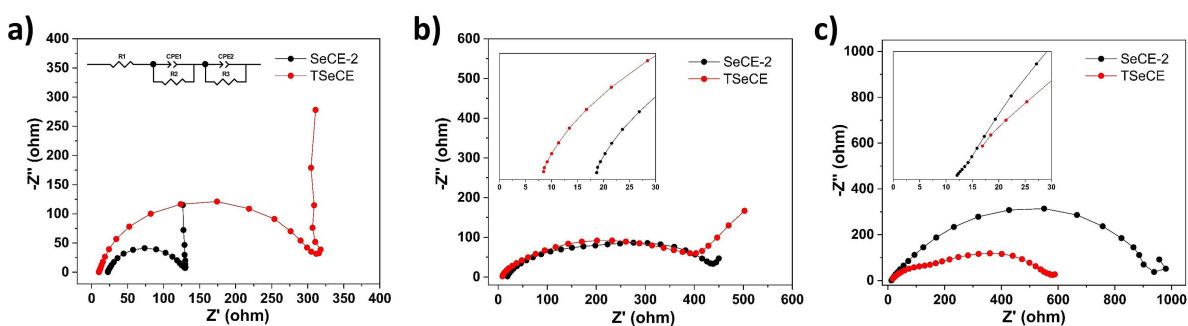


Figure 5. Nyquist plots of the SeCE-2 and TSeCE a) before cycling, b) after discharge and c) after charge with inset pictures showing the intercepts in the high-frequency regions.

increasing. The unstable charge transfer resistance could be caused by the local high selenium loading due to the non-uniform distribution of selenium during repeated cycles.

3. Conclusions

In this study, a binder-free selenium nanowires/CNT composite electrode was synthesized by using a facile chemical method. The selenium loading and thickness of the composite electrode are adjustable by regulating the amounts of reactants. The SEM and EDS results show that the thickness of the composite electrode has a critical impact on distribution of selenium in the electrode during repeated cycles, and then affect the electrochemical performance of the electrode. By decreasing the thickness to 23 μm , at selenium content of 60% in the entire electrode, the binder-free Se/CNT electrode exhibits high discharge capacity of 537 mAhg^{-1} (79% of the theoretical capacity) at 1 C and long cycling stability with a small capacity fading of 0.03% per cycle over 500 cycles at 1 C. This study reveals that the uniformity of the distribution of selenium in the electrode not only in the original state but also during the repeated cycles is critical to the cycling performance. Thin electrodes result in uniform distribution of selenium in both discharged and charged states, leading to the promising cycle life of the binder-free Se/CNT electrode.

Experimental Section

Materials

Lithium bis(trifluoromethanesulfonimide) (LiTFSI, LiN(CF₃SO₂)₂, 99%, Acros Organics), lithium nitrate (LiNO₃, 99.999%, Acros Organics), 1,2-dimethoxyethane (DME, 99.5%, Sigma Aldrich), 1,3-dioxolane (DOL, 99.8%, Sigma Aldrich), ethanol (Anhydrous, Fisher Scientific), selenium oxide (SeO₂, 99.8%, trace metal basis, Acros Organics), beta-cyclodextrin (β -cyclodextrin, 98%, Acros Organics), ascorbic acid (C₆H₈O₆, LabChem), long multiwalled carbon nanotubes (CNTs, length: 30–100 μm , 95 + %, Nanostructured & Amorphous Materials, Inc.) and medium multiwalled carbon nanotubes (CNTs, length: 10–50 μm , 95 %, Nanostructured & Amorphous Materials, Inc.) were purchased and used as received.

Preparation of Electrolyte

The electrolyte is composed of 1.0 M LiTFSI and 0.2 M LiNO₃ in a mixture solvent of DME and DOL (1:1 v/v).

Preparation of Selenium Nanowire/CNT Composite Cathode

Selenium nanowires/CNT composite cathode was synthesized according to the literature with some modifications. In this study, two set of the selenium nanowires/CNT composite electrodes were prepared. Firstly, ascorbic acid was dissolved in de-ionized water to render a 0.03 M solution. The first set of composite electrodes with different selenium nanowires loadings were synthesized in this study by adjusting the reactant amounts. SeO₂ (0.25 g and 0.35 g) and β -cyclodextrin (0.25 g and 0.35 g), respectively, were added into a glass beaker with adjunction of 50 mL de-ionized water. The

mixture was magnetically stirred to fully dissolve. Then 60 mg CNTs (30 mg long CNTs/ 30 mg medium CNTs) was added into the clear solution, followed by adding 500 mL anhydrous ethanol. The mixture was vigorously stirred for about 10 min, and then it was ultrasonicated by using a Sonics vibracell VC505 sonicator for 5 min for dispersion. The prepared ascorbic acid solution (48 mL and 68 mL, respectively) was added into this mixture under continuous stirring. After reacting for 24 h, the mixture was ultrasonicated for 10 min causing the selenium nanowires and CNTs to interweave. The products were vacuum filtered onto a 7-cm-diameter filter paper and washed repeatedly with de-ionized water and anhydrous ethanol for several times. The formed cathode was a free-standing and flexible film. The cathode was dried under vacuum at 40–45 °C for 24 h to yield the selenium nanowires/CNT composite film. The film was cut into ~0.97 cm² discs (D=11 mm) and transferred into an Ar-filled glovebox for further handling and testing. The synthesized composite electrodes are named SeCE-1 and SeCE-2 corresponding to the reactant amounts of SeO₂ of 0.25 g and 0.35 g, respectively. The other set of the thin composite electrode was prepared by using SeO₂ and β -cyclodextrin (0.35 g/0.35 g) as reactants, and ascorbic acid solution (68 mL) with CNTs (30 mg/30 mg) following the same procedure. While doing the vacuum filtration, only 33.3% of the prepared product (~200 mL prepared selenium/CNTs in water/ethanol mixture solution) was filtered to form a thin composite electrode. It was named as TSCE corresponding to the reactant amounts of SeO₂ of 0.35 g. The TSCE was also cut into ~0.97 cm² discs (D = 11 mm) and transferred into an Ar-filled glovebox for further handling and testing.

Cell Fabrication and Electrochemical Evaluation

When assembling cells using the thick composite electrodes (SeCE-1 and SeCE-2), CR2032 Coin cells were used and cells were fabricated in an Ar-filled glove box. First, 15 μL electrolyte was added into the prepared composite electrode. Then a Celgard 2400 separator was placed on the top of the electrode followed by adding 15 μL electrolyte on the separator. Finally, a piece of lithium metal and nickel foam as a spacer was placed on the separator. The cell was crimped and taken out of the glove box for electrochemical evaluation. While assembling cells using the thin composite electrodes (TSCE), they were followed by the same procedure except for changing the added electrolyte to 10 μL on both sides.

Cells were galvanostatically cycled on an Arbin BT2000 battery cycler at different C rates (1 C=678 mA g^{-1} , based on the mass of material in the cells) and in voltage ranges (C/10 and C/5: 1.8–2.8 V, C/2: 1.75–2.8 V, 1 C and 2 C: 1.7–2.8 V, 3 C, 4 C and 5 C: 1.65–2.8 V). Cyclic voltammetry (CV) was performed on a BioLogic VSP potentiostat. The potential was swept from open circuit voltage to 1.8 V and then swept back to 2.8 V at a scanning rate of 0.02 mV s^{-1} .

Characterization

Thermogravimetric analysis (TGA) and differential scanning calorimetry (DSC) was performed on a TA 2000 instruments SDT Q600 analyzer. All the samples are between 5–7 mg and tested under Air flow at 50 mL min^{-1} while heating from 80 to 600 °C with temperature ramping rate of 5 °C min⁻¹.

The morphological characterization of the selenium nanowires/CNT composite cathode was conducted with a JEOL JSM-7800F field emission scanning electron microscopy (SEM). The elemental mapping was performed with energy-dispersive X-ray spectroscopy

(EDS) attached to the SEM at 7 kV to confirm the presence of selenium and carbon in the electrodes. The transmission electron microscope (TEM) images were taken by a JEOL 2100 field emission TEM at 200 kV.

The X-ray diffraction (XRD) data of the pristine electrode, discharged electrode, and charged electrode were collected on a Bruker D8 Discover XRD Instrument equipped with Cu K α radiation. The scanning rate was 1.2° min $^{-1}$, for 2 θ between 20° and 70°. The cycled electrode samples were obtained by opening the cells and rinsed by pure DME in the glovebox. Then the electrodes were dried in the chamber under vacuum and protected with Kapton tape.

Acknowledgements

This work was supported by the US National Science Foundation under Grant No. 1603847, and the startup grant from Purdue School of Engineering and Technology and Department of Mechanical and Energy Engineering at Indiana University-Purdue University Indianapolis. We would also like to acknowledge the Integrated Nanosystems Development Institute (INDI) for use of their Bruker D8 Discover XRD Instrument, which was awarded through the NSF grant MRI-1429241 and for use of their JEOL7800F Field Emission SEM, which was awarded through NSF grant MRI-1229514. Use of the Center for Nanoscale Materials, an Office of Science user facility, was supported by the U.S. Department of Energy, Office of Science, Office of Basic Energy Sciences, under Contract No. DE-AC02-06CH11357.

Conflict of Interest

The authors declare no conflict of interest.

Keywords: chemical synthesis • composite material • lithium-selenium batteries • nanowires • selenium cathode

- [1] a) M. Armand, J.-M. Tarascon, *Nature* **2008**, *451*, 652; b) J. B. Goodenough, K.-S. Park, *J. Am. Chem. Soc.* **2013**, *135*, 1167.
- [2] a) A. Manthiram, *J. Phys. Chem. Lett.* **2011**, *2*, 176; b) J. B. Goodenough, *Energy Environ. Sci.* **2014**, *7*, 14.
- [3] a) P. G. Bruce, S. A. Freunberger, L. J. Hardwick, J.-M. Tarascon, *Nat. Mater.* **2012**, *11*, 19; b) A. Manthiram, Y. Fu, S.-H. Chung, C. Zu, Y.-S. Su, *Chem. Rev.* **2014**, *114*, 11751.
- [4] a) X. Ji, L. F. Nazar, *J. Mater. Chem.* **2010**, *20*, 9821; b) A. Rosenman, E. Markevich, G. Salitra, D. Aurbach, A. Garsuch, F. F. Chesneau, *Adv. Energy Mater.* **2015**, *5*, 1500212.
- [5] a) A. Manthiram, Y. Fu, Y.-S. Su, *Acc. Chem. Res.* **2012**, *46*, 1125; b) M. Barghamadi, A. Kapoor, C. Wen, *J. Electrochem. Soc.* **2013**, *160*, A1256; c) D. Eroglu, K. R. Zavadil, K. G. Gallagher, *J. Electrochem. Soc.* **2015**, *162*, A982; d) M. A. Pope, I. A. Aksay, *Adv. Energy Mater.* **2015**, *5*, 1500124.

- [6] a) Q. Pang, X. Liang, C. Kwok, L. F. Nazar, *J. Electrochem. Soc.* **2015**, *162*, A2567; b) N. Jayaprakash, J. Shen, S. S. Moganty, A. Corona, L. A. Archer, *Angew. Chem. Int. Ed.* **2011**, *50*, 5904; c) J. Liang, Z.-H. Sun, F. Li, H.-M. Cheng, *Energy Storage Mater.* **2016**, *2*, 76; d) Y. Xu, Y. Wen, Y. Zhu, K. Gaskell, K. A. Cychosz, B. Eichhorn, K. Xu, C. Wang, *Adv. Funct. Mater.* **2015**, *25*, 4312; e) Z. Li, J. Zhang, X. W. D. Lou, *Angew. Chem. Int. Ed.* **2015**, *54*, 12886.
- [7] a) J. Scheers, S. Fantini, P. Johansson, *J. Power Sources* **2014**, *255*, 204; b) J.-W. Park, K. Ueno, N. Tachikawa, K. Dokko, M. Watanabe, *J. Phys. Chem. C* **2013**, *117*, 20531; c) L. Suo, Y.-S. Hu, H. Li, M. Armand, L. Chen, *Nat. Commun.* **2013**, *4*, 1481; d) S. Kinoshita, K. Okuda, N. Machida, T. Shigematsu, *J. Power Sources* **2014**, *269*, 727; e) K. Dokko, N. Tachikawa, K. Yamauchi, M. Tsuchiya, A. Yamazaki, E. Takashima, J.-W. Park, K. Ueno, S. Seki, N. Serizawa, *J. Electrochem. Soc.* **2013**, *160*, A1304.
- [8] a) Y.-S. Su, A. Manthiram, *Nat. Commun.* **2012**, *3*, 1166; b) J. Park, B. C. Yu, J. S. Park, J. W. Choi, C. Kim, Y. E. Sung, J. B. Goodenough, *Adv. Energy Mater.* **2017**, *7*, 1602567; c) W. Kong, L. Yan, Y. Luo, D. Wang, K. Jiang, Q. Li, S. Fan, J. Wang, *Adv. Funct. Mater.* **2017**, *27*, 1606663; d) Y. C. Jeong, J. H. Kim, S. Nam, C. R. Park, S. J. Yang, *Adv. Funct. Mater.* **2018**, *28*, 1707411; e) M. M. U. Din, R. Murugan, *Electrochim. Commun.* **2018**, *93*, 109.
- [9] a) P. T. Dirlam, R. S. Glass, K. Char, J. Pyun, *J. Polym. Sci. Part A* **2017**, *55*, 1635; b) K. Park, J. H. Cho, J.-H. Jang, B.-C. Yu, T. Andreah, K. M. Miller, C. J. Ellison, J. B. Goodenough, *Energy Environ. Sci.* **2015**, *8*, 2389; c) J. Luo, R.-C. Lee, J.-T. Jin, Y.-T. Weng, C.-C. Fang, N.-L. Wu, *Chem. Commun.* **2017**, *53*, 963; d) J.-K. Huang, M. Li, Y. Wan, S. Dey, M. Ostwal, D. Zhang, C.-W. Yang, C.-J. Su, U.-S. Jeng, J. Ming, *ACS Nano* **2018**, *12*, 836.
- [10] a) A. Abouimrane, D. Dambourret, K. W. Chapman, P. J. Chupas, W. Weng, K. Amine, *J. Am. Chem. Soc.* **2012**, *134*, 4505; b) Y. Cui, A. Abouimrane, J. Lu, T. Bolin, Y. Ren, W. Weng, C. Sun, V. A. Maroni, S. M. Heald, K. Amine, *J. Am. Chem. Soc.* **2013**, *135*, 8047.
- [11] a) Y. Cui, A. Abouimrane, C.-J. Sun, Y. Ren, K. Amine, *Chem. Commun.* **2014**, *50*, 5576; b) C. P. Yang, S. Xin, Y. X. Yin, H. Ye, J. Zhang, Y. G. Guo, *Angew. Chem. Int. Ed.* **2013**, *52*, 8363; c) L.-C. Zeng, W.-H. Li, Y. Jiang, Y. Yu, *Rare Met.* **2017**, *36*, 339.
- [12] a) A. Eftekhar, *Sustainable Energy Fuels* **2017**, *1*, 14; b) Q. Li, H. Liu, Z. Yao, J. Cheng, T. Li, Y. Li, C. Wolverton, J. Wu, V. P. Dravid, *ACS Nano* **2016**, *10*, 8788; c) J. Jin, X. Tian, N. Srikanth, L. B. Kong, K. Zhou, *J. Mater. Chem. A* **2017**, *5*, 10110.
- [13] a) F. Wu, J. T. Lee, Y. Xiao, G. Yushin, *Nano Energy* **2016**, *27*, 238; b) J. T. Lee, H. Kim, M. Oschatz, D. C. Lee, F. Wu, H. T. Lin, B. Zdyrko, W. I. Cho, S. Kaskel, G. Yushin, *Adv. Energy Mater.* **2015**, *5*, 1400981; c) K. Han, Z. Liu, H. Ye, F. Dai, *J. Power Sources* **2014**, *263*, 85; d) Q. Cai, Y. Li, Q. Li, J. Xu, B. Gao, X. Zhang, K. Huo, P. K. Chu, *Nano Energy* **2017**, *32*, 1; e) S.-F. Zhang, W.-P. Wang, S. Xin, H. Ye, Y.-X. Yin, Y.-G. Guo, *ACS Appl. Mater. Interfaces* **2017**, *9*, 8759; f) X. Zhao, L. Yin, T. Zhang, M. Zhang, Z. Fang, C. Wang, Y. Wei, G. Chen, D. Zhang, Z. Sun, *Nano Energy* **2018**, *49*, 137; g) B. Kalimuthu, K. Nallathambi, *ACS Appl. Mater. Interfaces* **2017**, *9*, 26756; h) C. Luo, J. Wang, L. Suo, J. Mao, X. Fan, C. Wang, *J. Mater. Chem. A* **2015**, *3*, 555.
- [14] J. Zhang, Y. Xu, L. Fan, Y. Zhu, J. Liang, Y. Qian, *Nano Energy* **2015**, *13*, 592.
- [15] L. Zeng, W. Zeng, Y. Jiang, X. Wei, W. Li, C. Yang, Y. Zhu, Y. Yu, *Adv. Energy Mater.* **2015**, *5*, 1401377.
- [16] J. He, Y. Chen, W. Lv, K. Wen, P. Li, Z. Wang, W. Zhang, W. Qin, W. He, *ACS Energy Lett.* **2016**, *1*, 16.

Manuscript received: March 26, 2019

Accepted manuscript online: April 8, 2019

Version of record online: April 24, 2019